Supplementary Materials for Electron Ptychography Reveals Correlated Lattice Vibrations at Atomic Resolution

Anton Gladyshev, Benedikt Haas, Thomas C. Pekin, Tara M. Boland, Marcel Schloz, Peter Rez and Christoph T. Koch

June 23, 2025

Experimental Conditions

The 4D-STEM dataset of hexagonal boron nitride bicrystal was acquired in a Nion HERMES microscope using a single 256x256 pixel wide chip of Dectris ELA direct electron detector. The acquisition time, beam current, accelerating voltage, beam convergence semi-angle and the real-space scan step were set to 2 ms, 19 pA, 60 kV, 40 mrad and 30.4 pm, respectively. Diffraction patterns were recorded with a reciprocal sampling of 0.61 mrad per detector pixel. In total, 7 identical 4D-STEM datasets were acquired one after another at the same region of interest and a non rigid registration [1] was applied to eliminate the sample drift. One of these 7 datasets was used to perform the ptychographic reconstruction presented in this paper. In order to exclude inelastic scattering we further employed energy-filtering. In order to correct the geometric distortion created by the energy filter in the recorded diffraction patterns we acquired two tilt series with a small convergence semi-angle using the ELA detector (placed after the energy filter) and a detector placed before the filter. Using two tilt datasets we fitted a distortion vector field and applied an inverse transformation to the recorded diffraction patterns.

Theory

Strictly speaking, an iterative ptychographic algorithm fits a forward model that, for a given scanning position (two coordinates $\rho_{p,x}$ and $\rho_{p,y}$) maps an illumination wavefront to a measured diffraction pattern given in terms of spatial frequencies k_x and k_y. This model includes a transmission function of the investigated sample and can be formulated in various complexity levels. Recovering the initially unknown transmission function is the main goal of any ptychographic algorithm, as its amplitude characterizes absorption while its phase is directly proportional to the specimen's electrostatic potential. During the reconstruction one can additionally refine the probe [2–4], scan positions [3–5] or a mis-tilt angle between the optical axis of the microscope and the zone axis of the studied crystal [6].

When an electron beam passes through a sufficiently thin sample, it experiences only one scattering event. The three dimensional structure of an object can be simplified to two lateral dimensions by integrating over the beam propagation direction. For a beam position ρ_p, the exit wave $\psi^{(exit)}(\rho_p, \rho)$ becomes a real space product of a two-dimensional wave function of the incident beam $\psi^{(in)}(\rho - \rho_p)$ with a two-dimensional complex transmission function of a specimen $O(\rho)$. The corresponding diffraction pattern (far-field intensity) can be calculated as an absolute squared modulus of the Fourier transformed exit wave:

$$I(\rho_p, k) = \left| \mathcal{F}\left\{ \psi^{(exit)}(\rho_p, \rho) \right\} \right|^2 = \left| \mathcal{F}\left\{ \psi^{(in)}(\rho - \rho_p) \cdot O(\rho) \right\} \right|^2 . \tag{S1}$$

Increasing the beam wavelength and specimen thickness makes the effect of multiple scattering more pronounced. [7] showed that at some point the thin object approximation starts to fail. In this case the most efficient strategy is to ”divide and conquer”. Instead of using one two dimensional transmission function, one can split the propagation direction into multiple intervals and define a set of 2D transmission functions responsible for each particular sufficiently thin region. We can write

$$\psi_j^{(exit)}(\rho_p, \rho) = \psi_j^{(in)}(\rho - \rho_p) \cdot O_j(\rho), \tag{S2}$$

where j indicates a particular interval, i.e. slice. The propagation between the neighboring slices j and $j+1$ over the interval d is computed using a convolution with a Fresnel propagator:

$$\psi_{j+1}^{(in)}(\rho) = \mathcal{F}^{-1}\left\{\mathcal{F}\left\{\psi_j^{(exit)}(\rho)\right\} \cdot \mathcal{P}_{Fr}\left(k\right)\right\} \tag{S3}$$

$$\mathcal{P}_{Fr}\left(k\right) = exp\left[-i\pi\lambda d|k|^2\right], \tag{S4}$$

where λ is a wavelength of the electron beam and the equation S4 defines the Fresnel propagator in reciprocal space. Typically one chooses the distance between the slices of approximately 1 nm [7, 8]. The $\psi_{j=0}^{(in)}(\rho - \rho_p)$ is the incident illumination wavefront and for N slices the exit-wave $\psi_{j=N}^{(exit)}(\rho)$ is used to calculate a diffraction pattern as described in the equation S1. Often the beam propagation direction slightly deviates from the zone axis of a crystal. Then, the Fresnel propagator can be modified [6, 9] to compensate misalignment angles up to a few degrees. For two misalignment angles α_x and α_y along x and y axes, respectively, the tilted Fresnel propagator is defined as follows:

$$\mathcal{P}_{Fr}\left(k, \alpha_x, \alpha_y\right) = exp\left[-i\pi\left(\lambda d|k|^2 + 2k_x\alpha_x + 2k_y\alpha_y\right)\right]. \tag{S5}$$

In a real experimental situation, it is not always appropriate to neglect the partial spatial coherence of the electron source and vibrations of the atoms. To account for partial spatial coherence, Thibault and Menzel [10] proposed to replace the pure probe state $\psi_{j=0}^{(in)}(\rho)$ with a statistical mixture of multiple probe states $\psi_{j=0,m}^{(in)}(\rho)$, where the first index $j = 0$ remained from the multi-slice formalism and the second index m accounts for multiple modes. The total predicted diffraction pattern is calculated as an incoherent sum of the intensities corresponding to the individual probe modes. Let $I^{(1)}(\psi_{j=0}^{in}(\rho - \rho_p), O(\rho))$ denote the sequence of operations required to obtain a diffraction pattern from a single probe mode. In mixed-probe formalism, the intensity is modeled as

$$I_{total} = \frac{1}{N_{probe\ modes}} \sum_{m=0}^{N_{probe\ modes}} I^{(1)}(\psi_{j=0,m}^{in}(\rho - \rho_p), O(\rho)). \tag{S6}$$

The mixed-object formalism [10] is a natural extension of the mixed-probe formalism that accounts for a non-stationary object's transmission function. Due to the lattice vibrations and the corresponding displacements of the atoms, two electrons hitting the specimen at exactly the same spatial position but at two different points in time interact with slightly different electrostatic potentials. To account for this effect, i.e. thermal diffuse scattering (TDS) [11], one can use multiple transmission functions and model a diffraction pattern as an incoherent average of the intensities corresponding to the individual pure transmission functions.

$$I_{total} = \frac{1}{N_{object\ modes} \cdot N_{probe\ modes}} \sum_{n=0}^{N_{object\ modes}} \sum_{m=0}^{N_{probe\ modes}} I^{(1)}(\psi_{j=0,m}^{in}(\rho - \rho_p), O_n(\rho)). \tag{S7}$$

Thus, in the most complex scenario one has to deal with a three dimensional illumination wavefront (2 lateral dimensions plus one dimension for multiple modes), a four dimensional object (2 lateral dimensions and two dimensions one each for multiple slices and multiple modes) and perform $N_{object\ modes} \times N_{probe\ modes}$ forward multi-slice propagations to model one diffraction pattern.

Reconstruction Algorithm

We employ an in-house written code based on a python library CuPy [12]. All reconstructions were done on a single NVIDIA H100 GPU. Our ptychographic reconstruction is organized as a gradient-based minimization of a metric [3, 4, 13], i.e. a loss function, describing the discrepancy between the measured intensities I^m and the ones predicted by the forward model, as defined in the master equation S7 and further denoted as I. This study employs a Gaussian-likelihood metric [14]:

$$\mathcal{L}_{Gauss} = \sum \left(\sqrt{I^m} - \sqrt{I} \right)^2, \tag{S8}$$

where the sum goes over all beam positions and all pixels.

The loss derivative and corresponding update-vectors, are computed via Wirtinger calculus [15] a limited-memory BFGS (l-BFGS) algorithm [15, 16]. For simulated silicon data no additional regularization was employed and an initial guess for the object was created using uniform prior. The reconstruction show in Fig. 2e of the main text went in two stages: 1) A prior reconstruction with single object mode and 9 probe modes initialized using Hermite polynomials [7]; 2) Final reconstruction using a probe fitted during the first stage with 20 object modes. This scheme allows to apply a constraint on the recovered correlations by absorbing as much collective motion of the beam or sample during the first stage and recover the non-uniform vibrations during the second one.

The experimental hBN dataset was padded with zeros in reciprocal space up to a shape of 732×732 pixels resulting in a pixel size of ptychographic reconstruction of 10.89 pm. We further applied a $2/3$ frequency cutoff to all intermediate waves (i.e. between each slice) to prevent aliasing artifacts [9]. The reconstruction went in four stages: 1) initial reconstruction with single probe mode, single object mode and 30 object slices. This allowed us to estimate the aberrations of the beam. Further, cross-correlating the slices with their next neighbors allowed us to determine a minuscule difference between the zone axis of the crystal and the beam propagation direction. We used this value and adopted a tilted propagator [6] as defined in S5 without an additional refinement of the angle for all subsequent steps. 2) reconstruction with 10 probe modes and a single object mode without any regularization using the angle fitted during the stage 1; 3) 10 object modes were generated by adding uniform prior to the object recovered at the stage 2; 4) After the object at stage 3 was free from noise we added at the beginning, we applied regularization to the object, in particular, an l_1-regularization [3] of the absorption potential enforcing the amplitude of the retrieved transmission function to be closer to 1 and a missing-wedge regularization [6, 7] damping the high k_z Fourier-components at small k_x and k_y.

Undersampling of the Beam Propagation Direction

We would like to highlight an importance of accounting for multiple scattering when performing mixed-object ptychography. Reconstructions presented in the main text were done using slice thickness of 2 Å, but the corresponding simulations at 0.5 Å. The reason for such fine sampling in the reconstruction lies in the fact, that the effect of under-sampling along the beam propagation direction may be much more noticeable than the features produced by a particular type of atomic motion. We performed additional 4D-STEM simulations using same 30 MD snapshots of the silicon grain boundary but with an increased slice thickness. In Fig. S1 we show a gaussian-log likelihood (in arbitrary units) between one correlated dataset with slice thickness of 0.5 Å and another correlated dataset with a larger slice thickness. The gray dashed line shows Gaussian log-likelihood between correlated and uncorrelated datasets, both simulated using slice thickness of 0.5 Å. From the plot clearly follows that the difference between various kinds of interatomic vibrations is far weaker than the difference caused by under-sampling along the beam propagation direction. Further in Fig. S1b – d we show differences between position-averaged diffraction patterns (PACBED) of correlated and uncorrelated datasets, correlated and undersampled-correlated datasets, and correlated and perfectly coherent datasets, respectively.

References

1. O'Leary, C. M., Haas, B., Koch, C. T., Nellist, P. D. & Jones, L. Increasing spatial fidelity and SNR of 4D-STEM using multi-frame data fusion. *Microscopy and Microanalysis* **28,** 1417–1427 (2022).
2. Maiden, A. & Rodenburg, J. An improved ptychographical phase retrieval algorithm for diffractive imaging. *Ultramicroscopy* **109,** 1256–1262 (Oct. 2009).
3. Schloz, M. *et al.* Overcoming information reduced data and experimentally uncertain parameters in ptychography with regularized optimization. *Optics express* **28,** 28306–28323 (Sept. 2020).
4. Du, M. *et al.* Adorym: A multi-platform generic X-ray image reconstruction framework based on automatic differentiation. *Optics express* **29,** 10000–10035 (Mar. 2021).
5. Maiden, A., Humphry, M., Sarahan, M., Kraus, B. & Rodenburg, J. An annealing algorithm to correct positioning errors in ptychography. *Ultramicroscopy* **120,** 64–72 (June 2012).
6. Sha, H., Cui, J. & Yu, R. Deep sub-angstrom resolution imaging by electron ptychography with misorientation correction. *Science Advances* **8,** eabn2275 (May 2022).

7. Chen, Z. *et al.* Electron ptychography achieves atomic-resolution limits set by lattice vibrations. *Science* **372,** 826–831 (May 2021).
8. Brown, H. G. *et al.* A Three-Dimensional Reconstruction Algorithm for Scanning Transmission Electron Microscopy Data from a Single Sample Orientation. *Microscopy and Microanalysis* **28,** 1–9 (June 2022).
9. Kirkland, E. *Advanced Computing in Electron Microscopy* ISBN: 978-1-4419-6532-5 (June 2010).
10. Thibault, P. & Menzel, A. Reconstructing state mixtures from diffraction measurements. *Nature* **494,** 68–71 (Feb. 2013).
11. Loane, R. F., Xu, P. & Silcox, J. Thermal Vibrations in Convergent-Beam Electron Diffraction. *Acta Crystallographica Section A* **47,** 267–278 (May 1991).
12. Okuta, R., Unno, Y., Nishino, D., Hido, S. & Loomis, C. *CuPy: A NumPy-Compatible Library for NVIDIA GPU Calculations* in *Proceedings of the Workshop on Machine Learning Systems (LearningSys) at NeurIPS* (2017). `https://cupy.dev`.
13. Kronenberg, M., Menzel, A. & Guizar-Sicairos, M. Iterative least-squares solver for generalized maximum-likelihood ptychography. *Optics express* **26,** 3108–3123 (Feb. 2018).
14. Godard, P., Allain, M., Chamard, V. & Rodenburg, J. Noise models for low counting rate coherent diffraction imaging. *Optics express* **20,** 25914–25934 (Nov. 2012).
15. Wirtinger, W. Zur formalen Theorie der Funktionen von mehr komplexen Veränderlichen. *Mathematische Annalen* **97,** 357–375 (Nov. 1927).
16. Liu, D. & Nocedal, J. English (US). *Mathematical Programming* **45,** 503–528. ISSN: 0025-5610 (Aug. 1989).

Extended data figures

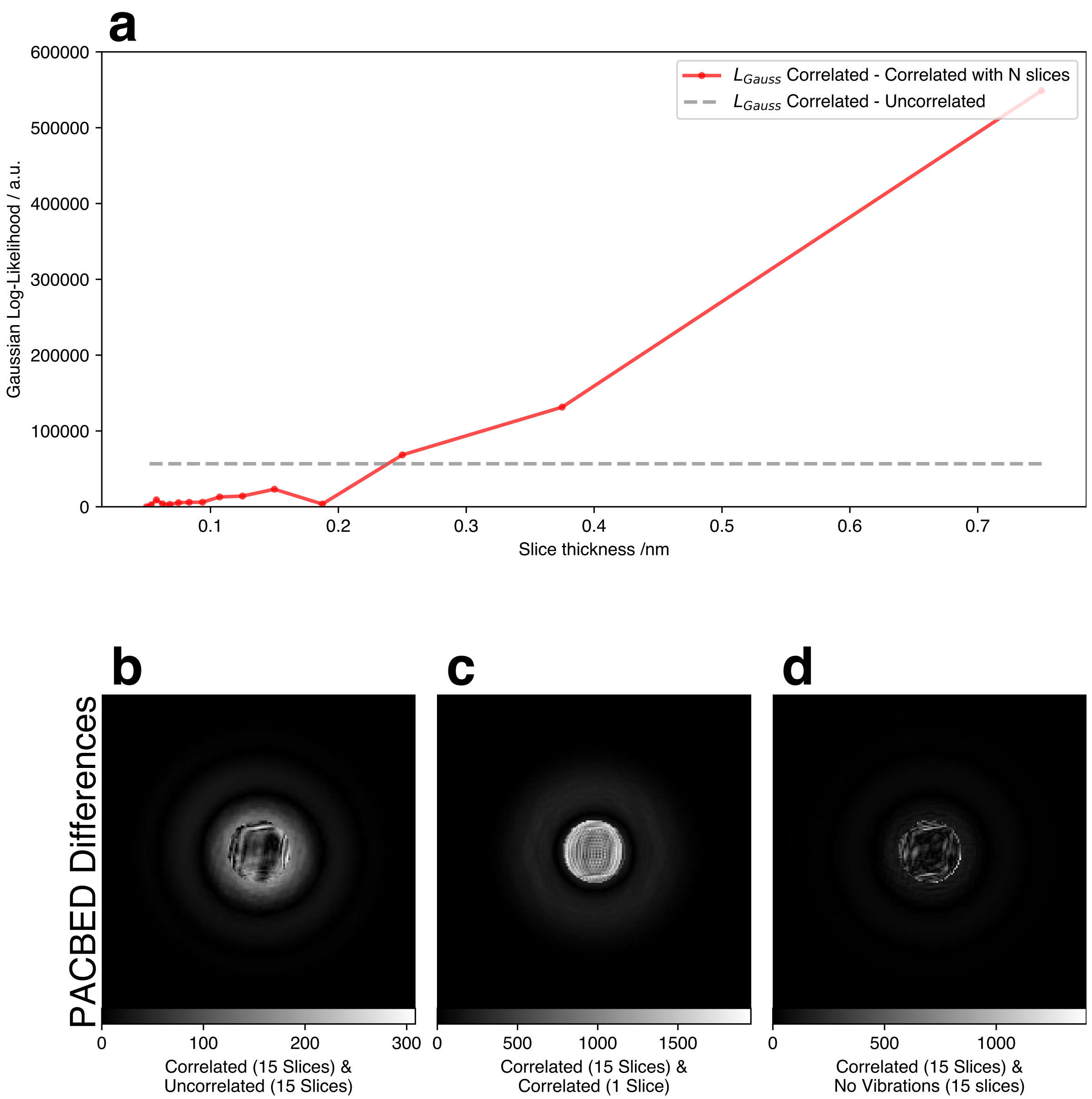

Fig. S1 | Effect of depth undersampling, i.e. of not sufficient slices along the beam propagation direction. Panel **a** shows the Gaussian log-likelihood between a fully sampled correlated 4D-STEM dataset (0.5 Å thick slices) of a symmetric $\Sigma 9$ grain boundary in silicon and multiple undersampled correlated datasets with increasing slice thickness (red), as well as between the correlated and uncorrelated datasets (gray dashed). Panels **b-–d** show PACBED difference maps comparing: **b** correlated vs uncorrelated, **c** correlated vs correlated-undersampled (15 slices), and **d** correlated vs absent vibrations data. Artifacts from undersampling exceed those caused by interatomic vibrations. Thus, to recover vibrations one should first account for effect of multiple scattering, even with a 0.7 nm thick sample.

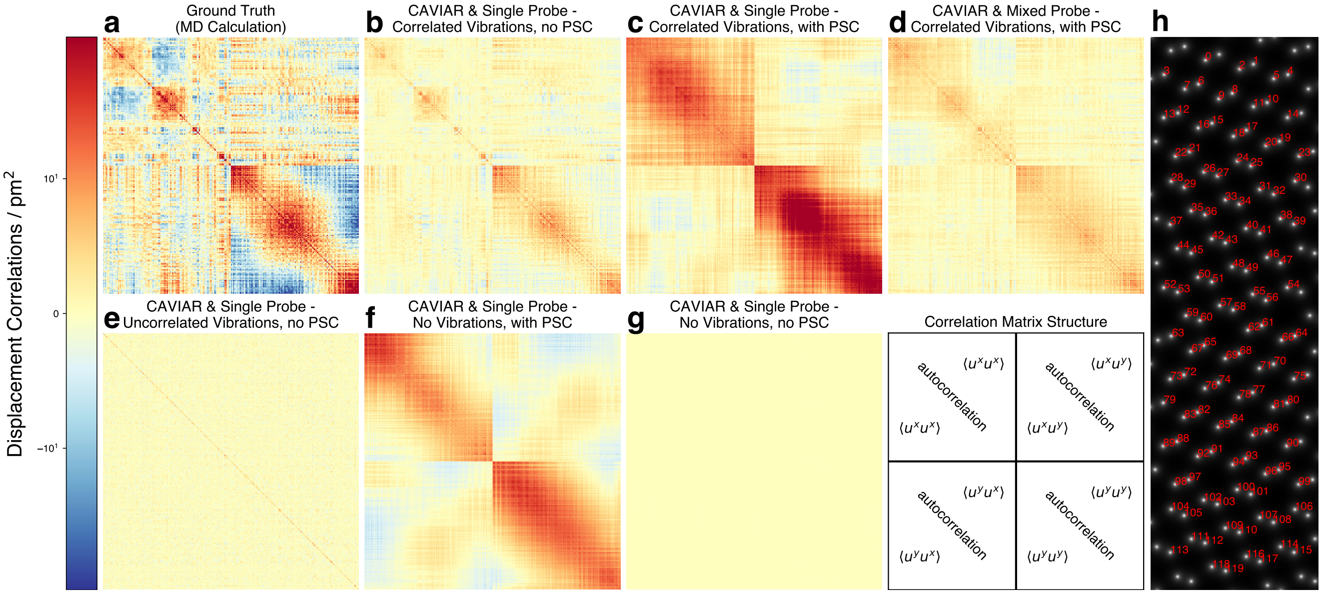

Fig. S2 | Full Green's tensors obtained via CAVIAR from various 4D-STEM datasets of a symmetric $\Sigma 9$ grain boundary in silicon. a, The ground truth correlation matrix derived from molecular dynamics simulations with clear off-diagonal structure indicating spatially correlated atomic displacements. **b,** The result of CAVIAR reconstruction from the dataset with correlated vibrations and no partial spatial coherence (PSC), preserving the main features of the ground truth but with slightly lower magnitude. **c,** CAVIAR reconstruction using a single probe mode from correlated dataset with additional partial spatial coherence, producing a structure similar to Panel **a** but offset by a uniform background. **d,** CAVIAR reconstruction from the same data as in **c**, but using 9 probe modes. Mixed probe efficiently mitigates the mentioned offset in correlations and produces correlations very similar to the ones shown in **a** and **b**. **e,** The reconstruction from a dataset based on the Einstein model without additional PSC, off-diagonal elements of the Green's tensor are close to zero indicating an absence of correlations between different degrees of freedom. **f,** A reconstruction from a dataset without any atomic vibrations but with partial spatial coherence (the dataset was not presented in the main text of the paper). The observed correlations stem from the incoherent illumination rather than atomic motion illustrating a positive offset mentioned the main text of the paper. **g,** The result for a perfectly static sample without PSC, where the correlation matrix exhibits near-zero values throughout, reflecting the absence of motion. In panel **h** we show indexing of atoms on top of a ground-truth phase. The structure of the matrices is schematically shown in the lower right corner. All CAVIAR reconstructions **b – g** except **d** used a single probe mode, in **d**, 9 incoherent probe modes were used.

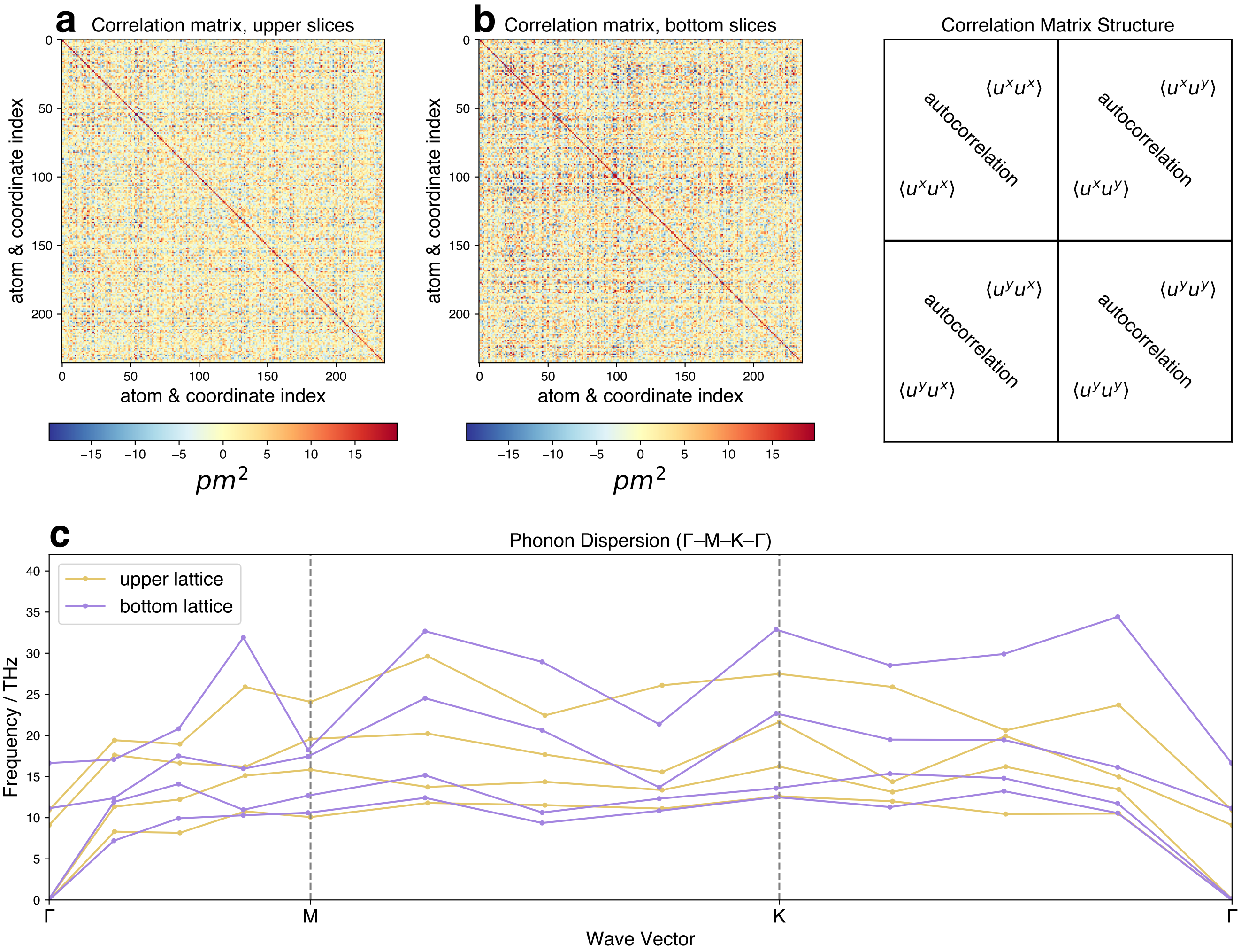

Fig. S3 | Interatomic correlations (Green's tensors) recovered from experimental mixed-object ptychographic reconstruction of approximately 15 nm thick bulk hBN crystal. Images **a** and **b** show average correlation matrices extracted from a z-range $z = 1.9$ nm $\ldots 5.7$ (top lattice) and $z = 8.6$ nm $\ldots 12.5$ nm (bottom lattice), respectively. The indices of the matrices run over all atoms in available in the field of view and two spatial coordinates (x, y), the structure of the matrices is schematically depicted on the right side. **c**, Phonon dispersion curves extracted from the reconstructed atomic displacement correlations using the lattice Green's tensor method from an experimental bulk hBN dataset. Yellow curves show the dispersion from the upper hBN lattice layer, and purple curves the one from the lower layer. Both are computed along the Γ-M–K-Γ direction of the Brillouin zone. The curves reveal acoustic and optical branches, although their absolute frequencies are reduced due to limited sampling of object states, limited spatial resolution and the lack of z-displacement sensitivity in the 2D projection. In the upper lattice the average frequencies along the $\Gamma - K - M - \Gamma$ path are 10.7 THz, 14.1 THz, 17.7 THz and 24.0 THz for transverse acoustic, longitudinal acoustic, transverse optical, longitudinal optical branches in upper lattice. For bottom lattice we get 10.8 THz, 13.0 THz, 18.2 THz, and 27.0 THz for the same four branches.